The link between morphology and structure of brightest cluster galaxies: automatic identification of cDs

Dongyao Zhao,[★] Alfonso Aragón-Salamanca and Christopher J. Conselice

School of Physics and Astronomy, The University of Nottingham, University Park, Nottingham NG7 2RD, UK

ABSTRACT

We study a large sample of 625 low-redshift brightest cluster galaxies (BCGs) and link their morphologies to their structural properties. We derive visual morphologies and find that ∼57 per cent of the BCGs are cD galaxies, ∼13 per cent are ellipticals, and ∼21 per cent belong to the intermediate classes mostly between E and cD. There is a continuous distribution in the properties of the BCG's envelopes, ranging from undetected (E class) to clearly detected (cD class), with intermediate classes (E/cD and cD/E) showing the increasing degrees of the envelope presence. A minority (∼7 per cent) of BCGs have disc morphologies, with spirals and S0s in similar proportions, and the rest (∼2 per cent) are mergers. After carefully fitting the galaxies light distributions by using one-component (Sérsic) and two-component (Sérsic+Exponential) models, we find a clear link between the BCGs morphologies and their structures and conclude that a combination of the best-fitting parameters derived from the fits can be used to separate cD galaxies from non-cD BCGs. In particular, cDs and non-cDs show very different distributions in the R_e–RFF plane, where R_e is the effective radius and RFF (the residual flux fraction) measures the proportion of the galaxy flux present in the residual images after subtracting the models. In general, cDs have larger R_e and RFF values than ellipticals. Therefore we find, in a statistically robust way, a boundary separating cD and non-cD BCGs in this parameter space. BCGs with cD morphology can be selected with reasonably high completeness (∼75 per cent) and low contamination (∼20 per cent). This automatic and objective technique can be applied to any current or future BCG sample with good-quality images.

Key words: galaxies: clusters: general – galaxies: elliptical and lenticular, cD – galaxies: structure.

1 INTRODUCTION

The brightest cluster galaxies (BCGs) are the most luminous and massive galaxies in today's Universe. Their stellar masses reach beyond ∼10^{11} M$_\odot$, and they reside at the bottom of the gravitational potential well of galaxy clusters and groups. Their formation and evolution relate closely to the evolution of the host clusters (Whiley et al. 2008) and further tie to the history of large-scale structures in Universe (Conroy, Wechsler & Kravtsov 2007). BCGs are typically classified as elliptical galaxies (Lauer & Postman 1992), but a fraction of them possess an extended, low-surface-brightness envelope around the central region. These are referred to as cD galaxies (e.g. Dressler 1984; Oegerle & Hill 2001).

The surface-brightness profile of elliptical galaxies was originally modelled using the empirical $r^{1/4}$ de Vaucouleurs law (de Vaucouleurs 1948). However, Lugger (1984) and Schombert (1986) showed that the $r^{1/4}$ model cannot properly describe the flux excess at large radii for most elliptical galaxies, and an additional parameter n was introduced in the so-called Sérsic ($r^{1/n}$) law (Sérsic 1963). For the most massive early-type galaxies, however, a single-Sérsic profile still does not reproduce their luminosity distribution accurately. Gonzalez, Zabludoff & Zaritsky (2005) found that a sample of 30 BCGs were best fitted using a double $r^{1/4}$ de Vaucouleurs profile rather than a single-Sérsic law. Furthermore, Donzelli, Muriel & Madrid (2011) suggested that a two-component model with an inner Sérsic and an outer exponential profile is required to properly decompose the light distribution of ∼48 per cent of the BCGs in their 430 galaxy sample. A similar conclusion was obtained by Seigar, Graham & Jerjen (2007).

The light profiles of BCGs need to be explained by any successful model of galaxy formation and evolution. In hierarchical models of structure formation, a two-phase scenario is currently favoured. Hopkins et al. (2009) proposed that an early central starburst could

★ E-mail: ppxdz1@nottingham.ac.uk

give rise to the bulge (elliptical) component of these galaxies, while the outer envelope was subsequently formed by the violent relaxation of stars originating in galaxies which merged with the central galaxy. Alternatively, Oser et al. (2010) and Johansson, Naab & Ostriker (2012) suggested that intense dissipational processes such as cold accretion or gas-rich mergers could rapidly build up an initially compact progenitor and, after the star formation is quenched, a second phase of slower, more protracted evolution is dominated by non-dissipational processes such as dry minor mergers to form the low-surface-brightness outskirts.

To shed light on the mechanism(s) leading to the formation of BCGs, especially of cD galaxies, we need to answer questions such as: Are elliptical and cD BCGs two clearly distinct and separated classes of galaxies? If so, are elliptical and cD BCGs formed by different processes or in different environments? Are the extended envelopes of cD galaxies intrinsically different structures which formed separately from the central bulge? To help answer these questions, in this paper we explore statistically how the visual classification of BCGs into different morphological classes (e.g. elliptical, cD; here referred to as 'morphology') relates to the quantitative structural properties of their light profiles (e.g. effective radius R_e, Sérsic-index n; generically called 'structure' in this paper). Moreover, finding an automatic and objective way to select cD BCGs is non-trivial for future data bases and study. Recent study such as Liu et al. (2008) identified cD BCGs by Petrosian parameter profiles (Petrosian 1976), but their method does not give an unambiguous criterion to separate cD galaxies from non-cD BCGs.

In this paper, we visually-classify 625 BCGs from the sample of von der Linden et al. (2007, hereafter L07) and fit accurate models to their light profiles. We find clear links between the visual morphologies and the structural parameters of BCGs, and these allow us to develop a quantitative and objective method to separate cDs galaxies from ellipticals BCGs. In a later paper (Zhao et al., in preparation), we will study how the visual morphology and structural properties of BCGs correlate with their intrinsic properties (stellar masses) and their environment (cluster mass and galaxy density), and explore the implications that such correlations have for the formation mechanisms and histories of cDs/BCGs.

The paper is organized as follows. In Section 2, we introduce the BCG samples and the visual morphological classification of the BCGs. In Section 3, we describe the light distribution models and the fitting methods we use, and discuss how the results are affected by sky-subtraction uncertainties. This section also presents a quantitative evaluation of the quality of the fits. In Section 4, we present the structural properties of the BCGs in the sample. In Section 5, we introduce an objective diagnostic to separate cDs from non-cD BCGs using quantitative information from their light profiles. We summarize our main conclusions in Section 6.

2 DATA

2.1 BCG catalogue and images

To study the structural properties of BCGs in galaxy groups and clusters, we use the BCG catalogue published by L07. The groups and clusters that host these BCGs come from the C4 cluster catalogue (Miller et al. 2005) extracted from the Sloan Digital Sky Survey (SDSS; York et al. 2000) third data release spectroscopic sample. The cluster-finding algorithm used to build the C4 catalogue identifies clusters as overdensities in a seven-dimensional parameter space of position, redshift, and colour, minimizing projection effects. The C4 catalogue gives a very clean widely-used cluster

sample which is well supported by simulations. Based on the C4 catalogue, L07 restricted their cluster sample to the $0.02 \leq z \leq 0.10$ redshift range to avoid problems related to the 55 arcsec 'fibre collision' region of SDSS. Within each cluster, L07 applied an improved algorithm to identify the BCG as the galaxy being closest to the deepest point of the potential well of the cluster (see L07 for a detailed discussion of this identification), and developed an iterative algorithm to measure the cluster velocity dispersion σ_{r200} within the virial radius R_{200}.[1] The catalogue created by L07 contains 625 BCGs in galaxy groups and clusters with redshifts $0.02 \leq z \leq 0.10$ spanning a wide range of cluster velocity dispersions, from galaxy groups ($\sigma_{r200} \leq 200$ km s^{-1}) to very massive clusters ($\sigma_{r200} \sim 1000$ km s^{-1}). 75 per cent of the BCGs in L07 are in dark matter haloes with $\sigma_{r200} \geq 309$ km s^{-1}, where the completeness of the haloes identified by the C4 algorithm is expected to be above 50 per cent. Obviously, for larger halo masses the completeness is higher.

The images we use to classify the BCGs and analyse their structural properties come from the SDSS Seventh Data Release (DR7) r-band images. We also use SDSS-DR7 g-band images of the BCGs in Section 4.1. The BCG catalogue used in this paper together with their main properties is presented in Appendix A.

2.2 Visual classification

The 625 BCGs in L07 sample were visually classified by careful inspection of the SDSS images. BCGs were displayed using a logarithmic scale between the sky level and the peak of the surface-brightness distribution. The contrast was adjusted manually to ensure that the low-surface-brightness envelopes were revealed if present. cD galaxies are identified by a visually extended envelope, while the envelope is not visible in our elliptical BCGs. Finally, the BCGs were classified into three main types: 414 cDs, including pure cD (356), cD/E (53), and cD/S0 (5); 155 ellipticals, including pure E (80), E/cD (72), and E/S0 (3); 46 disc galaxies, containing spirals (24) and S0s (22). The main morphological classes of BCGs are illustrated in Fig. 1. There are also 10 BCGs undergoing major mergers, but we will not discuss them in this paper in any detail.

Over half of the BCGs in the sample are classified as cDs. Separating cD BCGs and non-cD elliptical BCGs is a very hard problem since there is no sharp distinction between these two classes (e.g. Patel et al. 2006; Liu et al. 2008). Detecting the extended stellar envelope that characterises cD galaxies depends not only on its dominance, but also on the quality and depth of the images, and on the details of the method(s) employed. We used intermediate classes such as cD/E (probably a cD, but could be E) and E/cD (probably E, but could be cD) to account for the uncertainty inherent in the visual classification.

Our careful inspection of the images clearly reveals that there is a wide range in the brightness and extent of the envelopes. There seems to be a continuous distribution in the envelope properties, ranging from undetected (pure E class) to clearly detected (pure cD class), with the intermediate classes (E/cD and cD/E) showing increasing degrees of envelope presence. This continuous distribution in envelope detectability will also be made evident in the structural analysis carried out later in this paper. The classification we present here does not intend to be a definitive one since such a thing is probably unachievable. Our aim is to obtain a homogeneous and

---

[1] R_{200} is the radius within which the average mass density is $200\rho_c$, where ρ_c is the critical density of the universe.
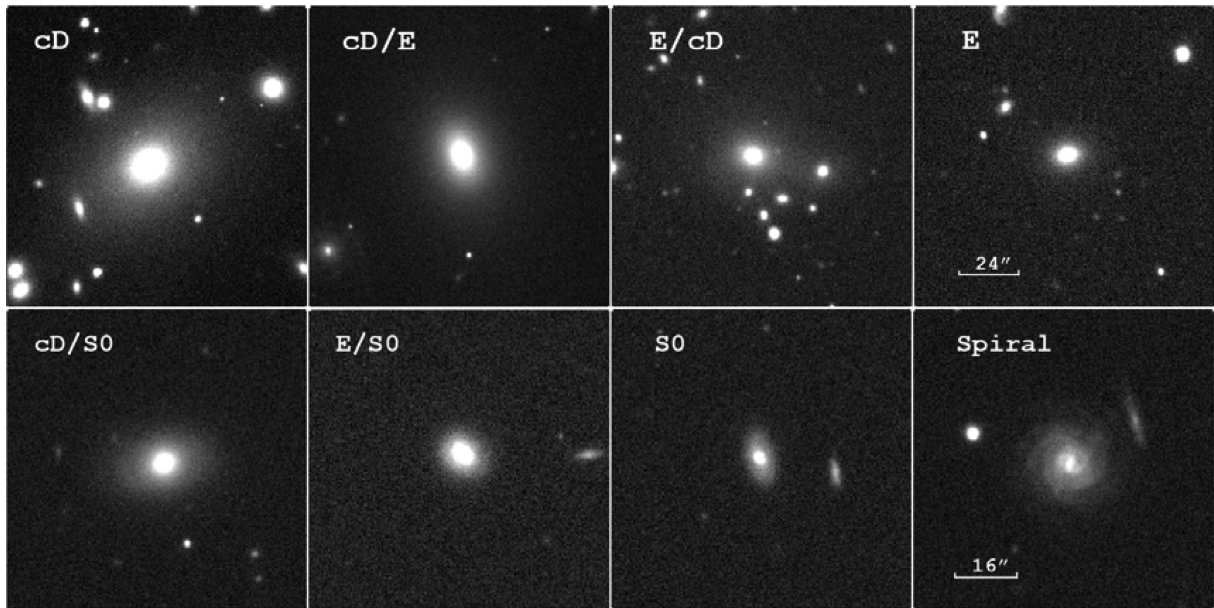
Figure 1. Examples of the main morphological classes of BCGs in our sample (cD, cD/E, E/cD, E, cD/S0, E/S0, S0, Spiral) illustrating the gradual transition between classes. The images are displayed using a logarithmic surface-brightness scale.

systematic visual classification of the BCGs and then study how such classification correlates with quantitative and objective structural properties of the BCGs. The visual morphological types of all the galaxies in the sample are presented in Appendix A.

We checked the effect that the redshift of BCGs may have on the visual classification. cDs might be mistakenly identified as elliptical if they are more distant since the extended low-surface-brightness envelope may be harder to resolve at higher redshifts. Fig. 2 illustrates the redshift distribution of the three main types. cD galaxies generally share the same redshift distribution with elliptical BCGs, especially at $z \geq 0.05$. At $z < 0.05$, we identify a slightly higher proportion (by ~ 10 per cent) of cD galaxies. However, if we compare the structural properties of cD and elliptical BCGs which are at $z \geq 0.05$, the results we obtain do not significantly differ from those using the full-redshift sample. As an additional check, we artificially redshifted some of the lowest redshift galaxies ($z \sim 0.02$–0.03) to $z = 0.1$, the highest redshift of the sample, taking into account cosmological effects such as surface-brightness dimming. Because the redshift range of the BCGs we study is very narrow, the effect on the images is minimal and does not have any significant impact on the visual classification. We are therefore confident that our visual classification is robust and that in the relatively narrow redshift range explored here any putative redshift-related biases will not affect our results.

3 QUANTITATIVE CHARACTERIZATION OF A BCG STRUCTURE

The surface-brightness profiles of galaxies provide valuable information on their structure and clues to their formation. It has become customary to fit the radial surface-brightness distribution using theoretical functions which have parameters that include a measurement of size (e.g. half-light radius or scalelength), a characteristic surface brightness, and other parameter(s) describing the shape and properties of the surface-brightness profiles. In this paper, we use GALFIT (Peng et al. 2002) to fit the 2D luminosity profile of each BCG using two parametric models, and thus determine the best-fitting parame-
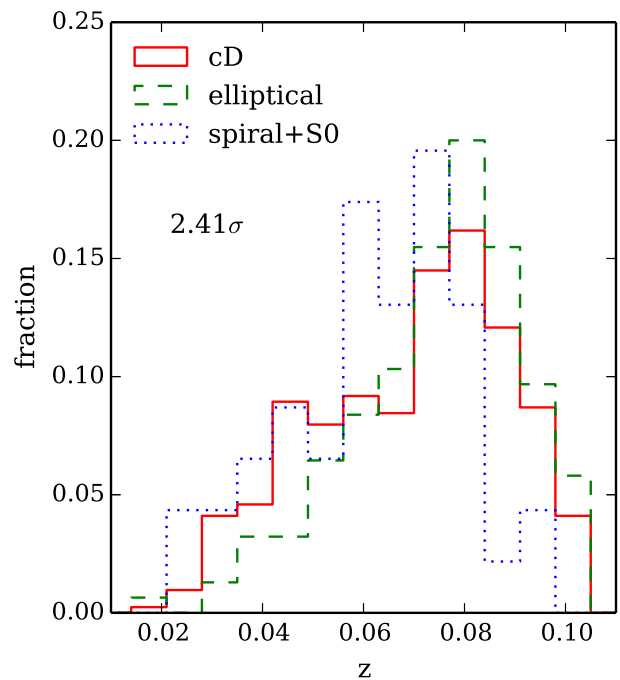

Figure 2. Redshift distribution for BCGs with different morphological types. The red solid line corresponds to cD BCGs, the green dashed line to ellipticals, and the blue dotted line to disc (spiral and S0) BCGs. A Kolmogorov–Smirnov test indicates that the redshift distributions of cD and elliptical BCGs are only different at the $\sim 2.4\sigma$ level. cD galaxies share the same redshift distribution with elliptical BCGs at $z \geq 0.05$, while there are proportionally ~ 10 per cent more cD galaxies at $z < 0.05$.

ters of each model. GALFIT can simultaneously fit model profiles to several galaxies in one image, which is particularly important for BCGs since they usually inhabit very dense environments. In this way, the light contamination from nearby galaxies can be accounted for appropriately.

We explore two models to represent the luminosity profile of the BCGs. A model commonly used to fit a variety of galaxy light profiles is the generalization of the $r^{1/4}$ de Vaucouleurs (1948) law introduced by Sérsic (1963). The Sérsic model has the form

$$I(r) = I_e \exp\{-b[(r/R_e)^{1/n} - 1]\}, \tag{1}$$

where $I(r)$ is the intensity at distance r from the centre, R_e, the effective radius, is the radius that encloses half of the total luminosity, I_e is the intensity at R_e, n is the Sérsic index representing concentration, and $b \simeq 2n - 0.33$ (Caon, Capaccioli & D'Onofrio 1993). The Sérsic function provides a good model for galaxy bulges and massive elliptical galaxies. Since BCGs are mostly early-type galaxies, it is reasonable to fit their structure with single-Sérsic models first. Subsequently, in order to explore the complexity introduced by the extended envelopes of cD galaxies, we will also fit the light profile of BCGs adding an additional exponential component to the Sérsic profile. Adding this exponential component is the simplest way to describe the 'extra-light' from the extended envelope. Note that the exponential profile $I(r) = I_0 \exp(-r/r_s)$ is just a Sérsic model with $n = 1$. The models assume that the isophotes have elliptical shapes, and the ellipticity and orientation of each model component are parameters determined in the fitting process.

In order to run GALFIT, we require a postage stamp image for each BCG with appropriate size to measure its structure over the full extent of the object, a mask image with the same size as the stamp image, an initial guess for the fitting parameters, an estimate of the background sky level, and a point spread function (PSF). Details on how these ingredients are produced and the fitting procedures are given below.

3.1 Pipeline for one-component fits: GALAPAGOS

We run GALFIT using the GALAPAGOS pipeline (Barden et al. 2012). GALAPAGOS has been successfully applied to a wide variety of ground- and space-based images (Häussler et al. 2007; van der Wel et al. 2012, 2014; Huertas-Company 2013; Lani et al. 2013). We applied the version of GALAPAGOS 1.0 to fit the SDSS r-band images of the BCGs in our sample. The starting point are SDSS images with a size of 2047 × 1488 pixels. For each BCG, the pipeline carries out four main tasks before running GALFIT itself: (i) detection of all the sources present in the image; (ii) cutting out the appropriate postage stamp and preparing the mask image; (iii) estimation of the sky background; (iv) preparation of the input file for GALFIT. After completing these tasks, GALAPAGOS will run GALFIT using the appropriate images and input parameters. We describe now these tasks in detail.

(i) Source detection: SEXTRACTOR (Bertin & Arnouts 1996) is used to detect galaxies in the SDSS images. A set of configuration parameters defines how SEXTRACTOR detects sources. The values of the SEXTRACTOR input parameters follow Guo et al. (2009): DETECT_MINAREA = 25, DETECT_THRESH = 3.0, and DEBLEND_MINCONT = 0.003. This set of parameters were tested to perform well on SDSS r-band images so that the bright and extended BCGs were isolated from other sources without artificially deblending them into multiple components. SEXTRACTOR also provides estimates of several properties for the target BCGs and nearby objects such as their magnitude, size, axis ratio, and position angle. These values are used to calculate the initial guesses of the model parameters that are needed as inputs by GALFIT.

(ii) Postage stamp creation: GALAPAGOS cuts out a rectangular postage stamp centred on the target BCG which will be used by

GALFIT as input image. We define the 'Kron ellipse' for a galaxy image as an ellipse whose semimajor axis is the Kron radius[2] (R_{kron}), with the ellipticity and orientation determined by SEXTRACTOR. The postage stamp size is determined in such a way that it will fully contain an ellipse 3.5 times larger than the Kron ellipse, i.e. its semimajor axis is $3.5R_{kron}$, and has the same ellipticity and orientation. The 3.5 factor represents a compromise between computational speed and ensuring that virtually all the BCG's light is included in the postage stamp. At this stage, a mask image is also created, identifying and masking out all pixels belonging to objects in the postage stamp which will not be simultaneously fitted by GALFIT. The aim is to reduce the computational time by excluding objects too far from the BCG or too faint to have any significant effect on the fit. Following Barden et al. (2012), an 'exclusion ellipse' is defined for each galaxy with a semimajor axis $1.5R_{kron} + 20$pixels, and the same ellipticity and orientation as the Kron ellipse. GALAPAGOS masks out all objects whose exclusion ellipse does not overlap with the exclusion ellipse of the target BCG. These objects are deemed to be too far away from the BCG to require simultaneous fitting. Furthermore, all objects more than 2.5 mag fainter than the BCG are also masked out since they are too faint to affect the BCG fit. The pixels that belong to these objects according to the SEXTRACTOR segmentation maps are masked out and excluded from the fits. All the remaining objects will be simultaneously fitted by GALFIT at the same time as the BCG. For a detailed description of this process and a justification of the parameter choice, see Barden et al. (2012).

(iii) Sky estimation: accurate estimates of the sky background level is crucial when fitting galaxy profiles, particularly when interested in the low-surface-brightness outer regions. Overestimating the sky level will result in the underestimation of the galaxy flux, size, and Sérsic index n, and vice versa. GALAPAGOS uses a flux growth curve method to robustly estimate the local sky background around the target galaxy. SDSS DR7 also provides a global sky value for the whole 2047 × 1488 image frame and local sky values for each galaxy. The SDSS PHOTO pipeline estimates the sky background using the median flux of all the pixels in the image after 2.33σ-clipping. However, according to the SDSS-III website, the version of PHOTO used in DR7 and earlier data releases tended to overestimate both the global and local sky values. The sky measurement is improved by SDSS-III in later data releases, but since we use the images from DR7 we cannot use the SDSS sky value with enough confidence. Häussler et al. (2007) demonstrated that the sky measurement that GALAPAGOS produces is highly reliable for single-band fits because it takes into account the effect of all the objects in the image. Therefore, in this study we use the local sky background estimated by GALAPAGOS. The accurate sky measurement provided by GALAPAGOS indicates that we can reach a surface-brightness limit in the r band of $\sim$27 mag arcsec^{-2}. This is deep enough to study the faint extended structures of BCGs. For each galaxy, its local sky background is included in the GALFIT input file and is fixed during the fitting procedure. Given the importance of accurate sky subtraction, in Section 3.2 we will carry out an explicit comparison of our results using SDSS and GALAPAGOS sky estimates.

(iv) GALFIT Input: GALAPAGOS produces an input file which includes initial guesses for the fitting parameters based on the SEXTRACTOR output. As mentioned above, all objects which are not masked out are fitted simultaneously using a Sérsic model. The

---

[2]In this paper, we use the following definition of 'Kron radius': $R_{kron} = 2.5r_1$, where r_1 is the first moment of the light distribution (Kron 1980; Bertin & Arnouts 1996). For an elliptical light distribution, this is, strictly speaking, the semimajor axis.

initial-guess model parameters for these nearby companions are also determined from SExtractor. In order to obtain reasonable results, we impose some constraints on the acceptable model parameter range. Our constrains on position, magnitude, axis ratio, and position angle follow Häussler et al. (2007). Additionally, the half-light radius R_e is constrained within $0.3 \leq R_e \leq 800$ pixels. This prevents the code from yielding unreasonably small or large sizes. Since the pixel size of the SDSS images is 0.396 arcsec, R_e is constrained to be larger than 0.12 arcsec, which is much smaller than the PSF, and smaller than half the size of the original input images, reasonable for the range of redshifts explored. In the original GALAPAGOS pipeline, the constraint on the Sérsic index is $0.2 \leq n \leq 8$. These are reasonably conservative limits, since normal galaxies with $n > 8$ are rarely seen and are often associated with poor model fits. However, some studies have shown that very luminous elliptical galaxies with $n > 8$ do exist (e.g. Graham et al. 2005), therefore for the target BCGs we allow n to be as large as 14 to keep the fits as free as possible. For the companion galaxies, which are fitted simultaneously, we still keep the constraint $0.2 \leq n \leq 8$. The final ingredient needed by GALFIT is a PSF image appropriate for each BCG. These are extracted from the SDSS DR7 data products[3] according to the photometric band used and the position of the BCG on the SDSS image.

3.2 Effect of the sky background subtraction: comparing SDSS and GALAPAGOS sky estimates

As described in Section 3.1, in this study we rely on the sky measurements provided by GALAPAGOS. However, it is important to test the effect that the choice of sky background has on our results. We do this by comparing the fitted Sérsic model parameters n and R_e using the GALAPAGOS and SDSS sky estimates. As mentioned before, SDSS DR7 provides a global sky value for the whole 2047×1488 image and local sky values for each galaxy. Guo et al. (2009) found that the local background estimates are generally larger than the global ones due to contamination from the outskirts of extended and bright sources, making them unreliable. We therefore restrict our comparison to the global SDSS sky values. We fit the BCG light profiles twice using exactly the same procedure and input parameters (see Section 3.1) but changing only the sky background estimates. The first set of fits use the GALAPAGOS-determined sky values, while the second set use the SDSS DR7 global ones.

Fig. 3 shows the distribution of the difference between the SDSS DR7 global sky and the sky measured by GALAPAGOS. It is clear that the SDSS global sky is generally larger than the local sky from GALAPAGOS. The effect from different sky values on the best-fitting structural parameters (Sérsic index n and effective radius R_e) is shown in Fig. 4. It is clear that the SDSS larger sky values result in the values of n_{sdss} and $r_{e,sdss}$ being smaller than the corresponding GALAPAGOS ones. The effect becomes more severe for those BCGs with large n and R_e, most of which are cD galaxies. This means the overestimated sky values would particularly affect the measurements on the low-surface-brightness envelopes of cD galaxies. Although it is difficult to know a priori which the *true* value of the sky background is, based on the fact that the SDSS-III provides evidence that DR7 sky values are overestimated while Häussler et al. (2007) showed reasonable proof of the reliability of the GALAPAGOS sky measurements, in what follows we will therefore trust and use the GALAPAGOS-determined sky values.
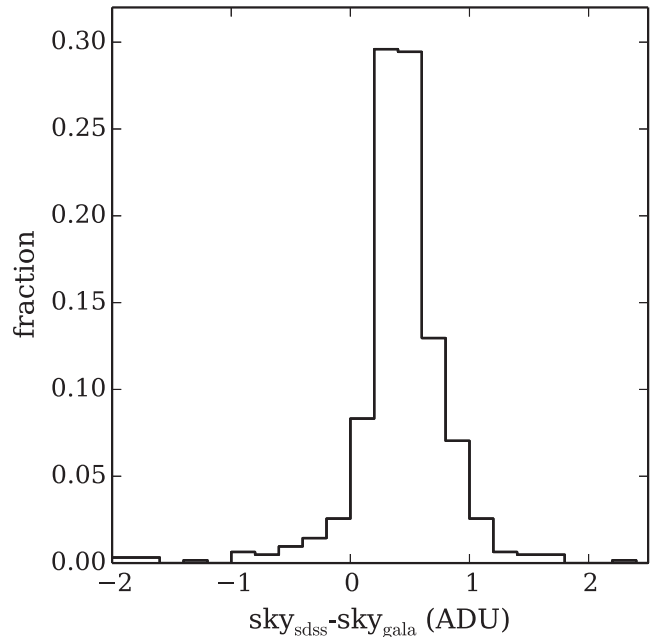
Figure 3. Distribution of the difference between the SDSS DR7 global sky and the GALAPAGOS-measured sky values. In general, SDSS overestimates the sky background. The average sky value measured by GALAPAGOS in the SDSS *r*-band BCG images is 140.8 ADU, corresponding to a surface brightness of $\sim$20.9 mag arcsec^{-2}.
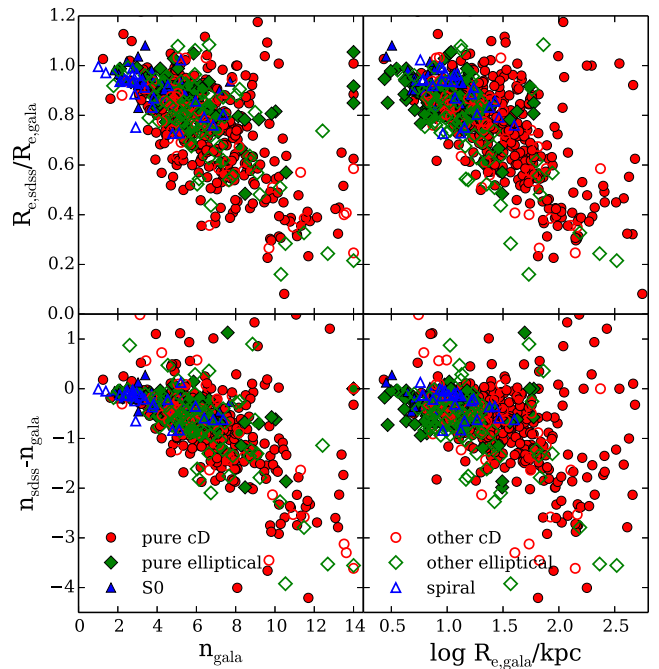

Figure 4. Comparison on the best fit n and R_e from single-Sérsic models using the SDSS and GALAPAGOS-measured sky estimates. Solid and open red circles correspond to pure cD and other cD galaxies (cD/E and cD/S0) respectively; solid and open green diamonds correspond to pure and other (E/cD and E/S0) elliptical BCGs respectively; solid blue triangles represent S0s and open ones are spirals. It shows that the SDSS overestimation of the global sky result in the values of n_{sdss} and $r_{e,sdss}$ being smaller than the corresponding GALAPAGOS ones. Moreover, the effect is more serious for the BCGs with large n and R_e which are mostly cDs.

3.3 Two-component fits

Although the light profiles of many early-type galaxies can be re-produces reasonably well with single-Sérsic models, the extended envelopes of cD galaxies may require an additional component. We therefore fitted all the BCGs by GALFIT using a two-component model consisting of a Sérsic profile plus an exponential. The input postage stamp, mask image, PSF, and sky values required by GALFIT remain the same as for the single-Sérsic fits. To ensure that we are fitting exactly the same light distribution, the location of the centre of the BCG is fixed to the *X*- and *Y*-coordinates determined in the single fit, and we also force the initial guesses of the model parameters to be the single-component fit results. The BCG companions are simultaneously fitted still with single-Sérsic profiles but with initial-guess parameters determined by the single-profile fits.

3.4 Residual flux fraction and reduced χ^2

Although the models we are fitting are generally reasonably good descriptions of the BCG light profiles, real galaxies can be more complicated, with additional features and structures such as star-forming regions, spiral arms, and extended haloes. It is therefore desirable to quantify how good the fits are and what residuals remain after subtracting the best-fitting models. A visual inspection of the residual images can generally give a good feel for how good a fit is, and sometimes tell us whether an additional component or components are required. However, more quantitative, repeatable, and objective diagnostics are also needed. The residual flux fraction (RFF; Hoyos et al. 2011) provides one such diagnostic. It is defined as

$$\mathrm{RFF} = \frac{\sum_{i,j \in A} |I_{i,j} - I_{i,j}^{\mathrm{model}}| - 0.8 \times \Sigma_{i,j \in A}\sigma_{i,j}^{\mathrm{bkg}}}{\Sigma_{i,j \in A}I_{i,j}}, \qquad (2)$$

where *A* is the particular aperture used to calculate RFF. Within *A*, $I_{i,j}$ is the original flux of pixel (*i,j*), $I_{i,j}^{\mathrm{model}}$ is the model flux created by GALFIT, and $\sigma_{i,j}^{\mathrm{bkg}}$ is the rms of the background. RFF measures the fraction of the signal contained in the residual image that cannot be explained by background noise. The 0.8 factor ensures that the expectation value of the RFF for a purely Gaussian noise error image of constant variance is 0.0. See Hoyos et al. (2011) for details. Obviously, this diagnostic can be applied to both single-Sérsic and two-component profiles, or any other model. The aperture *A* we use to calculate RFF is the 'Kron ellipse' defined in Section 3.1 (an ellipse with semimajor axis R_{kron} and the ellipticity and orientation determined by SEXTRACTOR for the BCG). $\Sigma_{i,j \in A}I_{i,j}$, the denominator of equation (2), is computed as the total BCG flux contained inside the Kron ellipse, which is one of the SEXTRACTOR outputs, and therefore independent of the model fit.

Since BCGs usually reside in dense environments, sometimes there are some faint nearby objects contained within the Kron ellipse that have not been fitted by GALFIT (those more than 2.5 mag fainter than the BCG, see Section 3.1). These objects will be present in the residual image. Moreover, brighter companions that have been simultaneously fitted may also leave some residuals due to inaccuracies in their fits. Therefore, even if the BCG light distribution has been accurately fitted, RFF can be affected by the residuals from the companion galaxies, failing to provide an accurate measure of the quality of the fit. To minimize the effect from companion galaxies on RFF, we mask out the pixels belonging to all companions within the Kron ellipse using SEXTRACTOR segmentation maps. The RFF will therefore measure the residuals from the BCG fit alone, excluding, as far as possible, those belonging to nearby galaxies.

An additional measurement of the fit accuracy is the reduced χ^2, which is minimized by GALFIT when finding the best-fitting models. It is defined as

$$\chi_\nu^2 = \frac{1}{N_{\mathrm{dof}}} \sum_{i,j \in A} \frac{(I_{i,j} - I_{i,j}^{\mathrm{model}})^2}{\sigma_{i,j}^2}, \qquad (3)$$

where *A* is the aperture used to calculate χ_ν^2, N_{dof} is the number of degrees of freedom in the fit, $I_{i,j}$ is the original image flux of pixel (*i, j*). $I_{i,j}^{\mathrm{model}}$ represents, for each pixel, the sum of the flux of the models fitted to all the galaxies in the aperture, and $\sigma_{i,j}$ is the noise corresponding to pixel (*i, j*). This noise is calculated by GALFIT taking into account the contribution of the Poisson errors and the read-out noise of the image (Peng et al. 2002).

Similarly to RFF, χ_ν^2 also measures the deviation of the fitted model from the original light distribution. The value of χ_ν^2 that GALFIT minimises to find the best-fitting model is calculated over the whole postage stamp, and includes contributions from all the objects fitted. To make sure that we only take into account the contribution to χ_ν^2 from the BCG fit, we calculate it within the Kron ellipse of the BCG, masking out the nearby objects as we did when calculating RFF.

The choice of aperture (Kron ellipse with semimajor axis of R_{kron}) over which we evaluate RFF and χ_ν^2 represents a good compromise between covering a large fraction of the galaxy light while minimizing the impact of close companions. We carried out several tests to evaluate the sensitivity of our results to the changes in aperture size. If we reduce the semimajor axis of the aperture by 20 per cent or more we lose significant information on the extended halo of BCGs, which we must avoid. If we increase the semimajor axis of the aperture by 20 per cent or more, we potentially increase the sensitivity to the galaxy haloes but in the crowded central cluster regions contamination from companion galaxies becomes a serious problem, generally increasing RFF and χ_ν^2. Changes in the aperture semimajor axis within ±20 per cent would have no effect on the conclusions of this paper.

3.5 Evaluating one-component and two-component fits

Since RFF and χ_ν^2 can quantify the residual images after subtracting the model fits, we attempt to use them to assess whether a one-component (Sérsic) fit or a two-component (Sérsic+Exponential) fit is more appropriate to describe the light profile of individual BCGs. In order to do this, we first evaluate the effectiveness of RFF and χ_ν^2 at quantifying the goodness-of-fit. We visually examine the fits and residuals obtained from both one- and two-component models for all the BCGs in our sample. In some cases, two of which are illustrated in Fig. 5, it is obvious which model is clearly favoured.

For those BCGs where such a clear distinction can confidently be made, we classify them into what we call 1C (one-component) BCGs and 2C (two-component) BCGs. Explicitly, 1C BCGs (e.g. galaxy 1 in the top panel of Fig. 5) are those for which a one-component Sérsic model represents their light distribution very well, and therefore the residuals left are small and show no significant visible structure. For these galaxies, adding a second component does not visibly improve the residuals. Conversely, 2C BCGs (e.g. galaxy 2 in the bottom panel of Fig. 5) are not well fitted by a one-component model, and the residuals are significant. These residuals often show excess light at large radii which can be identified as an exponential component or halo. Additionally, the fit to these galaxies visibly improves when using a two-component model. With these criteria, we confidently identify 53 1C BCGs
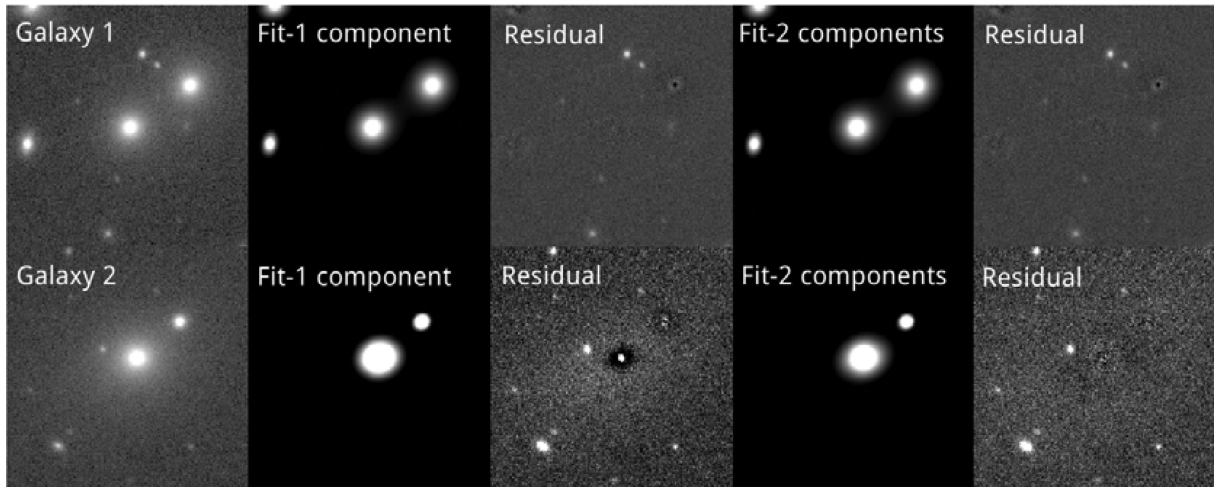
Figure 5. Example of one-component (Sérsic) fits and two-component (Sérsic+Exponential) fits for 1C and 2C BCGs, respectively. From left to right, the panels show the original image, the one-component model, the residuals after subtracting the one-component fit, the two-component model, and the residuals after subtracting the two-component fit. The upper panels show a 1C BCG where a one-component fit does a good job and adding a second component does not visibly improve the residuals. The lower panels show a 2C BCG, where the one-component residual exhibits clear excess light at large radii, suggesting that a second component is necessary. Indeed, the two-component residual is much better for this BCG.

and 25 2C BCGs. Since we want to test the sensitivity of RFF and χ_ν^2, we concentrate for now on this small but robust subsample. The rest of the BCGs (537) cannot be confidently classified into 1C or 2C BCGs because it is too hard to tell visually due to the residuals containing significant structures which cannot be accurately fitted by such simple models.

Fig. 6 presents a comparison of the RFF and χ_ν^2 values for the one- and two-component fits of the 53 1C BCGs and 25 2C BCGs. For 1C BCGs, the RFF and χ_ν^2 distributions of one- and two-component fits are virtually indistinguishable. Neither RFF nor χ_ν^2 improve significantly when the second component is added. However, RFF and χ_ν^2 are significantly smaller for the two-component fits of 2C BCGs. It is clear therefore that the quantitative information that RFF and χ_ν^2 provide agrees very well with the visual assessments of the fits. Both RFF and χ_ν^2 are sensitive to changes in the residuals, but RFF appears to be more sensitive. As shown in the bottom panels of Fig. 6, the improvement in the two-component fit for 2C BCGs is around 40–60 per cent when measured by RFF, while it is only ∼20 per cent when measured by χ_ν^2. A further useful piece of information obtained from this test is that the typical values of log RFF and log χ_ν^2 for fits deemed to be good by visual inspection are log RFF $\simeq -1.7^{+0.11}_{-0.06}$, and of log $\chi_\nu^2 \simeq 0.042^{+0.033}_{-0.025}$ (median +/− first and third quartiles of the parameter distributions).

As mentioned before, the majority of the BCGs cannot be visually classified into 1C or 2C BCGs with high certainty because their light distributions are too complex to be accurately represented by such simple models. Nevertheless, we can use the quantitative information provided by RFF and χ_ν^2 to gauge to what extent the BCGs are better fit by a two-component model than by a one-component model. This will be discussed later.

We would like to point out that this is the first time that the residual flux is calculated considering *only* the contribution of the target galaxies when estimating both RFF and χ_ν^2, explicitly excluding the contribution due to the companion galaxies. For instance, Hoyos et al. (2011) also used RFF to evaluate the goodness-of-fit, but they measured the residuals over all pixels within a specific area around the target galaxies, without excluding nearby companions. Similarly, the χ_ν^2 values from GALFIT have also been applied to evaluate which fitting model is better (e.g. Bruce et al. 2012), but the effect

of nearby objects on the χ_ν^2 values was also overlooked. Using the 2C BCG sample, we assessed the importance of this improvement. If the RFF and χ_ν^2 are calculated considering the residuals in all the pixels inside the relevant aperture, the RFF and χ_ν^2 distributions for the two-component fits of 2C BCGs cannot be distinguished from the one-component results. The effect of the contribution to the residuals from companion galaxies is so severe that it renders such a comparison useless. Our method therefore represents a significant step forward. It is extremely important to exclude the contribution of the companion galaxies when calculating RFF and χ_ν^2 in this kind of analysis.

4 STRUCTURAL PROPERTIES OF BCGs

Our morphologically-classified BCGs provide a large sample to statistically study their structural properties and link them to their morphological properties. In what follows we consider the three main morphological classes of BCGs: cDs (including all BCGs classified as pure cD, cD/E, and cD/S0); ellipticals (including pure E, E/cD, and E/S0), and disc (spiral and S0) BCGs. The 10 BCGs classified as mergers are excluded (see Section 2.2 for details). We decided to include the galaxies with 'uncertain' morphologies (such as cD/E and E/cD) in our analysis to reflect the difficulties involved in visual classification. However, to ensure the robustness of our analysis, at every stage we have checked that considering only 'pure' cD and elliptical BCGs (i.e. excluding the cD/E, cD/S0, E/cD, and E/S0 classes) would not change our conclusions.

Since most BCGs are early-type galaxies, we will first consider and discuss single-Sérsic models when fitting their SDSS *r*-band images. We will subsequently use Sérsic+Exponential models to see whether the fits are improved. But before embarking in the analysis of the parameters derived from these model fits, we first evaluate their uncertainties.

4.1 Structural parameter uncertainties

The parameter uncertainties that GALFIT reports are calculated using the covariance matrix derived from the Hessian matrix computed by the Levenberg–Marquardt algorithm that the program uses (Peng
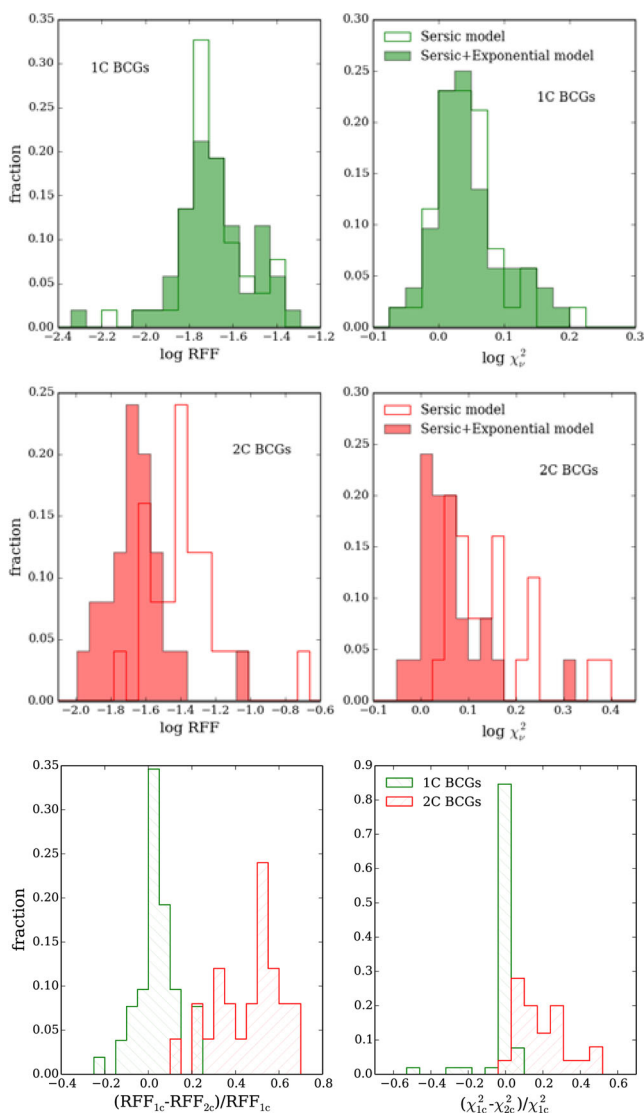
Figure 6. The top four panels show the distribution of log RFF (left) and log χ_ν^2 (right) for single-Sérsic (open histograms) and Sérsic+Exponential (solid histogram) fits. The two uppermost panels correspond to the 53 1C BCGs, while the middle panels correspond to the 25 2C BCGs. The two bottom panels show the difference in RFF and χ_ν^2 between one-component and two-component models for both sets of BCGs. Clearly, the RFF and χ_ν^2 distributions of one- and two-component fits are virtually indistinguishable for 1C BCGs. However, RFF and χ_ν^2 tend to be significantly smaller for the two-component fits of 2C BCGs. Typical values for good fits are log RFF $\simeq -1.7^{+0.11}_{-0.06}$, and log $\chi_\nu^2 \simeq 0.042^{+0.033}_{-0.025}$ (median +/− the first and third quartiles of the parameters). Both RFF and χ_ν^2 are sensitive to the magnitude of the residuals, but RFF is appears to be significantly more sensitive.

et al. 2010). These formal uncertainties are only meaningful when the model provides a good fit to the image, in which case the fluctuations in the residual image are only due to Poisson noise. However, for real galaxy images the residual images contain not only Poissonian noise, but also systematics from non-stochastic and stochastic factors due to additional components not included in the fitting function (e.g. spiral arms, star-forming regions), asymmetries, shape mismatch, flat-fielding errors and so on. These non-random factors usually dominate the uncertainty of the parameters, and the uncertainties inferred from the covariance matrices are only lower-limit

estimates (Peng et al. 2010). Therefore, if we rely on the errors reported by GALFIT the uncertainties in the structural parameters of the BCGs could be severely underestimated. Indeed, these formal errors seem unrealistically small: typical GALFIT uncertainties for R_e and n are only ∼1–2 per cent. A more robust and realistic way of determining these uncertainties is clearly needed.

We have measured the structural parameters of the BCGs in our sample using the SDSS *r*-band images. Independent measurements can also be obtained using the SDSS *g*-band images. In principle, the structural parameters could be wavelength dependent. However, the $g − r$ colours of massive early-type galaxies with old stellar populations are quite spatially uniform and do not change much from galaxy-to-galaxy (e.g. Fukugita, Shimasaku & Ichikawa 1995). Furthermore, morphological *k*-corrections are negligible for early-type galaxies between these two bands (e.g. Taylor-Mager et al. 2007), so it is reasonable to expect that the intrinsic structural parameters will not change much between *g* and *r* bands. Therefore, any differences in the measured parameters between these two bands should be largely dominated by measurement errors. Moreover, if there are significant wavelength-dependent differences in the measured parameters that are driven by real physical differences, it is reasonable to expect that these may correlate with other galaxy properties such as their colour, morphology, redshift, cluster velocity dispersion, etc. No such correlations were found, so we are confident that the intrinsic differences are not significant in these two bands.

We use GALAPAGOS to fit the SDSS *g*-band images of the BCGs in our sample in exactly the same way as we did for the *r*-band images. Fig. 7 shows a comparison of the R_e and RFF$_{1c}$ values obtained in both bands. Similar comparisons were carried out for the rest of the structural parameters. The scatter around the 1-to-1 relations is due, in principle, to both intrinsic wavelength-dependent differences and measurement errors. Since, as we have argued, the intrinsic differences are not expected to be significant between these two bands, the measurement errors should dominate the scatter. We can thus use this scatter as an estimate of realistic, albeit perhaps marginally pessimistic, parameter uncertainties. The average errors are $\delta(n) \simeq 0.9$, $\delta(\log R_e) \simeq 0.16$, and $\delta(\log \text{RFF}_{1c}) \simeq 0.13$.

The right-hand panel of Fig. 7 shows that the errors in R_e and RFF are not correlated. This is an important point since these two are the main parameters that we will use as diagnostics in our analysis in Section 5.

4.2 Single-Sérsic models

We analyse now the behaviour of four parameters derived from the best-fittng single-Sérsic models along with the morphological classifications. Two of them, the Sérsic index n and the effective radius R_e, provide information on the intrinsic properties of the BCGs. The other two, RFF and χ_ν^2, show how well the models fit the real light distribution of the BCGs and also provide information about their detailed structure. The values of these parameters are listed in Appendix A. Fig. 8 shows the distribution of these parameters for the three main BCG morphologies. The σ value in each panel indicates the significance (confidence level) of the observed differences between the cD and elliptical BCG parameter distributions. These are derived from two-sample Kolmogorov–Smirnov (K–S) tests.

4.2.1 Sérsic index n

The Sérsic index n measures the concentration of the light profile, with larger n corresponding to higher concentration. The upper-left
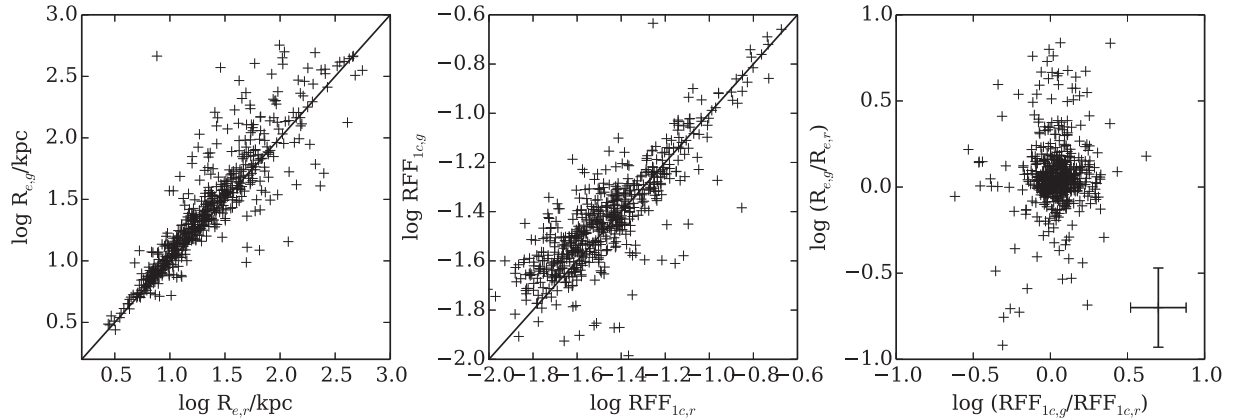
Figure 7. Comparison of the R_e (left-hand panel) and RFF_{1c} (middle panel) values obtained in both the SDSS g- and r bands. The solid lines correspond to the 1-to-1 relations. The right-hand panel shows $\log(R_{e,g}/R_{e,r})$ versus $\log(RFF_{1c,g}/RFF_{1c,r})$. The error bars in the bottom-right corner are derived from the rms scatter of each parameter.
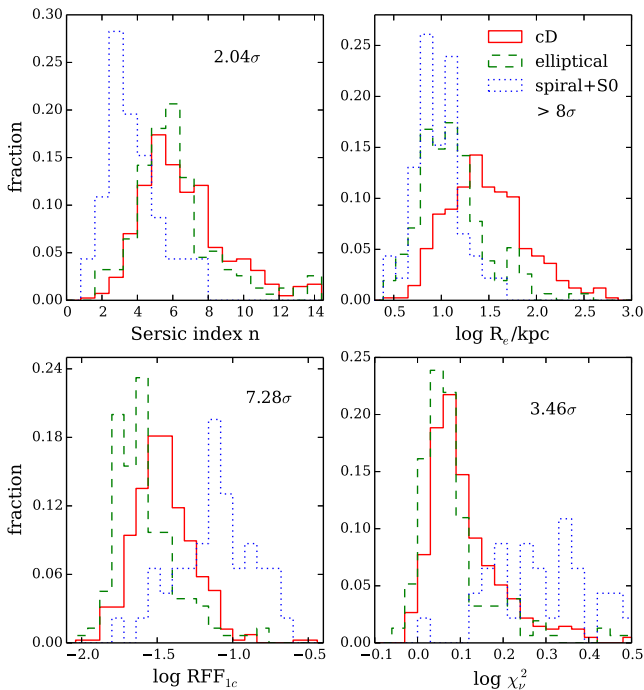

Figure 8. Distribution of the Sérsic index n (upper left), effective radius R_e (upper right), $\log RFF_{1c}$ (lower left), and $\log \chi_\nu^2$ (lower right) from single-Sérsic fits for the BCGs divided by morphology. The red solid line corresponds to cD galaxies, the green dashed line to ellipticals, and the blue dotted line to spirals and S0s. The σ value in each panel indicates the significance (confidence level) of the observed differences between the cD and elliptical BCG parameter distributions. These are derived from two-sample Kolmogorov–Smirnov tests.

panel of Fig. 8 presents the n distributions for the three main BCG morphologies. It is clear that disc (spiral and S0) BCGs tend to have smaller values of n, as expected. However, the n distribution for disc BCGs is skewed towards larger values ($n \gtrsim 3$) than those of the normal disc galaxy population (e.g. $n = 2.5$ in Shen et al. 2003). This is because most disc BCGs are early-type bulge-dominated spirals and S0s. Elliptical and cD BCGs tend to have larger n values ($n \geq 4$). The n distributions of cD and elliptical BCGs are quite similar. A K–S test indicates that the distributions are not significantly different: the significance of any possible difference is just 2.04σ.

4.2.2 Effective radius R_e

The effective radius R_e is a measurement of the extent (or size) of the light distribution. The upper-right panel of Fig. 8 shows the distributions of $\log R_e$. Disc BCGs tend to have relatively small sizes, and the vast majority of them ($\sim$85 per cent) have R_e smaller than $\sim$15 h^{-1} kpc. About 75 per cent of the elliptical BCGs also have $R_e \lesssim 15\,h^{-1}$ kpc, while cD galaxies tend to be significantly larger. More than 60 per cent of cDs have $R_e \gtrsim 15\,h^{-1}$ kpc. A K–S test demonstrates that the difference in R_e distributions between cD and elliptical BCGs is very significant. This suggests that R_e could be a good discriminator to separate cD and elliptical BCGs.

4.2.3 Residual flux fraction and reduced χ^2

The lower-left panel of Fig. 8 presents the RFF_{1c} distributions in a $\log_{10}$ scale, where RFF_{1c} denotes RFF for one-component models. The RFF_{1c} of disc BCGs has a much broader distribution and reaches significantly larger values than those of cDs and ellipticals. This reflects the fact that a single-Sérsic model is not a good representation of the light distribution of galaxies with clear discs, spiral arms, and star-forming regions. Early-type BCGs have smoother light distributions that can be reasonably well reproduced with a Sérsic profile, and their RFF_{1c} tend to be smaller. However, there are statistically significant differences between the RFF_{1c} distributions of cD and elliptical BCGs. About 60 per cent of elliptical BCGs have RFF_{1c} values in the range corresponding to good fits (see Section 3.5 and Fig. 6), while just $\sim$25 per cent of cD galaxies do. This suggests that most elliptical BCGs can be well represented by single-Sérsic models, while most cD galaxies are harder to model with such a simple profile. Since an extended envelope is a general property of cD galaxies, their deviation from a single-Sérsic profile may be due, at least partially, to this extended envelope. This suggests that an additional model component may be required for them. We will re-visit two-component models in Section 4.3. The clear difference in RFF suggests that RFF could be another good discriminator to separate cD and elliptical BCGs.

Similar conclusions can be reached from the distributions of χ_ν^2 shown in the lower-right panel of Fig. 8, albeit less clearly. This is not surprising since, as shown in Section 3.5, both RFF and χ_ν^2 measure the strength of the residuals, but χ_ν^2 is significantly less sensitive. Therefore, RFF is expected to be more efficient for separating cD and elliptical BCGs than χ_ν^2.

These results show a clear link between the visual morphologies of BCGs and their structural properties. Although cD galaxies tend to have similar shapes to elliptical BCGs, they usually have larger sizes and their structures generally deviate more from single-Sérsic profiles. In contrast, elliptical BCGs tend to be smaller, and their light profiles are statistically more consistent with single-Sérsic models. These structural differences, especially in R_e and RFF, could therefore provide quantitative ways to separate elliptical and cD BCGs without relying on visual inspection. We will explore these issues in Section 5.

4.3 Sérsic+Exponential models

The RFF distributions shown in Section 4.2 indicate that elliptical BCGs are statistically better fitted by a single-Sérsic model than cDs. Since a distinctive feature of cD galaxies is their extended luminous halo, two-component models may be more appropriate to describe accurately the light distributions of cD BCGs. Following Seigar et al. (2007) and Donzelli et al. (2011), we explore here how a model consisting of an inner Sérsic profile and an outer exponential envelope performs when fitting BCG images. The fitting process was described in detail in Section 3.3.

As shown in Section 3.5, both RFF and χ^2 can provide quantitative information to assess whether BCGs are better fitted by a two-component model than by a one-component model, at least in very clear cases. Fig. 9 shows a comparison of these parameters obtained for single-Sérsic and Sérsic+Exponential models. In the left-hand panel, we show a histogram of the fractional differences in the RFF values $(RFF_{1c} - RFF_{2c})/RFF_{1c}$ for all three BCG types. The right-hand panel shows the corresponding χ^2_ν fractional differences $(\chi^2_{\nu,1c} - \chi^2_{\nu,2c})/\chi^2_{\nu,1c}$. It is clear that for disc BCGs, the Sérsic+Exponential model does a better job. This is not surprising since spiral and lenticular galaxies contain clearly distinct bulges and discs. For elliptical BCGs, the improvement in RFF and χ^2_ν for two-component models is generally quite small, as expected: elliptical galaxies are known to be reasonably well fitted by Sérsic models, so the extra component does not improve the residuals significantly. Perhaps surprisingly, the improvement is also only marginally better for cDs: the typical fractional differences for cD galaxies are $(RFF_{1c} - RFF_{2c})/RFF_{1c} = 0.11^{+0.14}_{-0.08}$ and $(\chi^2_{\nu,1c} - \chi^2_{\nu,2c})/\chi^2_{\nu,1c} = 0.035^{+0.053}_{-0.029}$ (median +/− first and third quartiles of the parameter distributions).

Since the distributions shown in Fig. 9 for ellipticals and cDs are statistically indistinguishable, there is no clear separation that could be used to distinguish elliptical and cD BCGs by comparing one-component and two-component fits. Moreover, on average, Sérsic+Exponential model does not fit the profile of cD BCGs clearly better than single-Sérsic model. The reason is that for cD BCGs the values of RFF and χ^2_ν are generally not dominated by the presence or absence of a second exponential model component but by other structures present in the residual images, such as double cores. Since there is no clear improvement in the Sérsic+Exponential model, the model with the smallest number of parameters (i.e. single-Sérsic model) will be preferred for simplicity. The following discussions are based on the results from the single-Sérsic fits.

4.4 Summary of Section 4

In this section, we have analysed the differences in the structural properties of BCGs as a function of morphology. These structural parameters have been derived from one-component (Sérsic) and two-component (Sérsic+Exponential) model fits. Disc BCGs (a small minority) have smaller Sérsic indices (n) than elliptical and cD BCGs, as expected. They also have different, generally broader, distributions of RFF and χ^2_ν. Elliptical and cD BCGs have similar n values, but cDs tend to have larger values of R_e, RFF and χ^2_ν. These differences do not depend strongly on whether we use one- or two-component models.

The observed structural differences could provide quantitative ways to separate elliptical and cD BCGs without relying on visual inspection. We explore these in Section 5. Furthermore, the differences we have found in the structural parameters suggest that the formation histories of elliptical and cD BCGs may be different. For instance, gas-rich major mergers and other dissipative processes may be responsible for building the inner (Sérsic-like) component, while dissipationless minor mergers may contribute to the build-up of the outer extended envelope and to the growth of galaxy sizes (e.g. Oser et al. 2010; Johansson et al. 2012; Huang et al. 2013). We will explore in a subsequent paper (Zhao et al., in preparation) whether the morphological and structural properties of BCGs are linked to other intrinsic BCG properties such as their stellar mass, and/or to the properties of their environment. These links will provide more clues to the formation history of cDs/BCGs.

5 SEPARATING ELLIPTICAL AND CD BCGS

The results of Section 4.2 suggest that we may be able to use the different distributions of cD and non-cD BCGs on the $\log R_e$–$\log RFF_{1c}$ plane to separate them in an objective, quantitative and automatic way. Fig. 10 shows that cDs are clearly segregated from other BCGs in this two-dimensional parameter space. We attempt to find a robust, well-defined way to separate, statistically, cD and non-cD BCGs using the information provided by this diagram. In other words, we suppose to find an 'optimal border' that can separate them.

5.1 Method description and the optimal border

Ideally, any process that selects cD galaxies from a sample of BCGs needs to have high completeness (i.e. select as many of the cDs present in the sample as possible), while avoiding contamination from non-cDs (i.e. maximizing the purity of the sample). These two requirements compete with each other, and increasing completeness
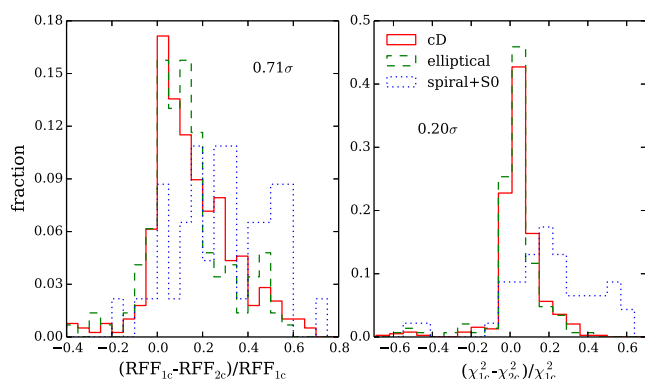

Figure 9. Comparison of the residuals between single-Sérsic and Sérsic+Exponential models. The left-hand panel shows the fractional differences in RFF obtained with two-component and one-component fits for cD (red solid line), elliptical (green dashed line), and disc (blue dotted line) BCGs. The right-hand panel shows the corresponding fractional differences for χ^2_ν.
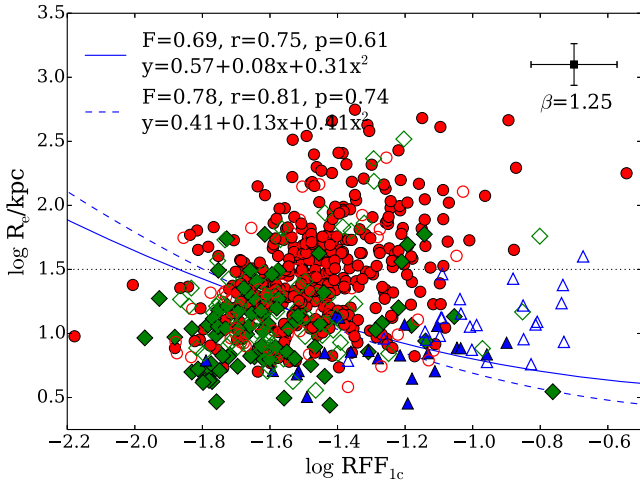
Figure 10. $\log R_e$ versus $\log \mathrm{RFF}_{1c}$ for the BCGs in our sample. We use this diagram to find the optimal border to separate cD from non-cD BCGs. The symbols are the same as in Fig. 4. The black dotted line is the 'first guess' for the border. The blue solid curve is the optimal border determined when we consider all cD BCGs (cD, cD/E and cD/S0) as cD galaxies. The blue dashed curve is the optimal border determined when we consider only pure cD and pure elliptical BCGs (excluding all cD/E, cD/S0, E/cD, E/S0, spiral and S0 BCGs). The legend shows the maximum F-score for the optimal borders and the corresponding completeness r and specificity p. The equations defining the optimal borders are also shown. The error bar shows the mean error of each parameter. We used $\beta = 1.25$ in this case.

often results in a decrease in sample purity, and vice versa. We need therefore to find the best compromise between these competing requirements. In general, the optimal solution will depend on the specific intent for the selected sample, and therefore on the decision of how much weight to give to completeness and to purity. It is useful to define a measurement on the quality of the selection method that combines both requirements in a well-defined way. The optimal solution will then be obtained by maximizing this quality parameter.

Following Hoyos et al. (2012) the *sensitivity*, which is often known as *completeness* in astronomy, is defined as

$$r = \frac{\# \text{ True Positives}}{\# \text{ True Positives} + \# \text{ False Negatives}}. \quad (4)$$

Similarly, we define *specificity* as

$$p = \frac{\# \text{True Negatives}}{\# \text{ True Negatives} + \# \text{False Positives}}. \quad (5)$$

A 'True Positive' is an object retrieved by the selection process with the required properties (i.e. a cD galaxy that is correctly selected as such). A 'False Negative' is an item that is not retrieved by the selection process but does present the needed properties (a cD galaxy that is not selected). A 'True Negative' is an item that is rightfully rejected by the selection process since it does not have the required properties (for instance, an elliptical galaxy that is not selected as a cD). A 'False Positive' is an item that is incorrectly picked up by the selection process, but does not have the properties of interest (for example, an elliptical galaxy that is wrongly selected as a cD).

Sensitivity and *specificity* can be combined into a single number, known as the *F-score* (van Rijsbergen 1979), which provides a single measure on the quality of the selection process. The *F*-score is just a weighted harmonic average of r and p,

$$F_\beta = \frac{(1 + \beta^2) \times p \times t}{\beta^2 \times p + r}, \quad (6)$$

where β is a control parameter that regulates the relative importance of completeness with respect to specificity. This is a user-supplied value that depends on the particular goals of the study. We will explore later how the choice of β affects our selecting results. At this stage, a value of $\beta = 1.25$ is used, which can be thought of as weighing completeness more than the lack of contamination. For our BCG samples, the *F*-score is used to grade the performance of the diagnostics we use when separating cD galaxies from the parent population.

The selection process that we will apply to the parent population of BCGs in order to select cD galaxies will be defined by a 'border' in the $\log R_e$–$\log \mathrm{RFF}_{1c}$ plane (see Fig. 10). This border will be represented by a second-order polynomial in the horizontal coordinate. Higher-order polynomials (or more complex functions) could be used, but the additional complexity is not required here. In our specific problem, the cD galaxies play the role of the 'items presenting the required properties' discussed above, and the parent population is the complete sample of BCGs.

According to the definition of *sensitivity* and *specificity*, the BCGs in the parent sample are classified into four categories by their position relative to the border. In the $\log R_e$–$\log \mathrm{RFF}_{1c}$ plane, cD galaxies dominate the region of large R_e and RFF_{1c}. We therefore define this region as the 'cD side'. Thus

(i) cD galaxies that fall on the cD side of the border are True Positives.

(ii) cD galaxies that do not fall on the cD side of the border are called False Negatives.

(iii) Elliptical and disc (spiral and S0) BCGs that fall on the cD side are regarded as False Positives.

(iv) Elliptical and disc (spiral and S0) BCGs that do not fall on the cD side of the border are True Negatives.

The optimal border is found by maximizing the *F*-score value. Following the method described in Hoyos et al. (2012), we use the Amoeba algorithm (Press & Spergel 1988) to carry out this maximization and find the polynomial defining the border.

It is clear from Fig. 10 that the selected galaxy sample on the cD side of the optimal border will not contain only cD galaxies, and a degree of contamination will be present. We define contamination (Hoyos et al. 2012) as

$$C = \frac{\#\text{non-cDs tested as positive}}{\#\text{all positives}}. \quad (7)$$

The numerator are the non-cD BCGs which are on the cD side of the optimal border. The denominator of this fraction includes both cD galaxies and non-cD BCGs on the cD side.

Fig. 10 shows the $\log R_e$–$\log \mathrm{RFF}_{1c}$ plane for the BCGs in our sample. The Amoeba algorithm requires a first guess for the border, shown by the black horizontal dotted line. The optimal border determined by the algorithm does not depend on the exact initial guess. The blue solid curve is the optimal border determined when we consider all cD galaxies (cD, cD/E, and cD/S0) as cD galaxies. This border, computed using $\beta = 1.25$, has *F*-score = 0.69. 75 per cent of all the cD galaxies are above the border ($r = 0.75$), and thus selected from the parent sample. The remaining 25 per cent are mixed with the elliptical and disc BCGs in the region below the border. This selection therefore yields 75 per cent completeness. The galaxy sample above the border contains 311 cD galaxies and 79 non-cD BCGs resulting in an ∼20 per cent contamination in the selected cD samples. In the region below, the border there are 103 cD galaxies and 122 and non-cD BCGs. Thus, the non-cD BGC sample has a contamination of 46 per cent from cD galaxies. This indicates that
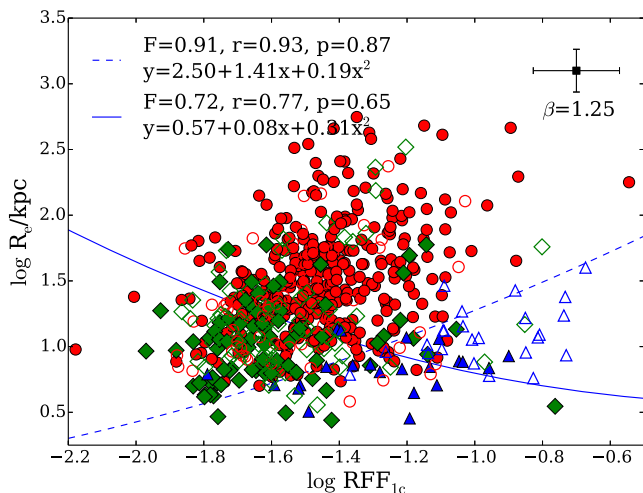
Figure 11. Two-step process to select cD BCGs. Symbols and legend are the same as in Fig. 10. Disc (spiral and S0) BCGs are separated from non-disc BCGs (cDs and ellipticals) first using the optimal border shown as the blue dashed curve. cD galaxies are then selected using the optimal border shown as the blue solid curve. See the text for details.

this technique is more effective (cleaner) at selecting cD galaxies than at selecting non-cD BCGs.

Note that if we consider a 'cleaner' sample that contains only pure cD and pure elliptical BCGs (excluding all cD/E, cD/S0, E/cD, E/S0, spiral, and S0 BCGs), the optimal border (blue dashed curve in Fig. 10) does not change significantly, but the quality of the selection as determined by the F-score value, the completeness r and the specificity p improves. This is not surprising: the identification of BCGs as pure cDs/Es (as opposed to the 'dubious' ones) depends on more secure morphological characteristics which should be linked more clearly to the structural parameters. However, considering only this cleaner sample is not a realistic scenario since in practical cases we would like to start from a full sample of BCGs and find which ones are cDs. Nevertheless, it is reassuring that the border we determine does not depend very strongly on the exact training set used.

On the selected cD side, spiral BCGs are an important source of contamination. However, since most of them appear in the large RFF_{1c} region, it would be possible to go a step further to implement a simple further refinement in our method to separate spirals from the selected cDs: very few cD galaxies have $\log RFF_{1c}$ larger than ~ -1.1. This would significantly improve the purity of the cD sample at very little cost in terms of its completeness.

Moreover, it is clear from Fig. 10 that all disc BCGs (spirals and S0s) contribute significantly to the contamination of either the cD or the elliptical samples separated by the best border. However, we can use the fact that disc BCGs distribute over a distinct area on the $\log R_e$–$\log RFF_{1c}$ plane to apply a two-step process to exclude them from our cD selection. First, the disc BCGs can be separated from the elliptical and cD BCGs, and then the cD BCGs can be selected out of the rest BCG sample. Fig. 11 illustrates the results of this two-step selection. The blue dashed curve is the optimal border determined in the first step. By excluding disc BCGs using this border, a very complete ($r = 0.93$) and pure ($p = 0.87$) non-disc BCG sample is built. The cDs can then be separated from the ellipticals using the optimal border shown by the blue solid curve with a completeness of 77 per cent (305 cDs are selected), and a contamination of only 14 per cent. Compared to the single-step cD selection (311 cDs were selected with 20 per cent contamination),

the two-step process clearly selects a very similar number of cDs but with better purity. The decision on whether the increase in purity is worth the additional complexity is left to the reader. In the reminder of this paper, we will use the single-step selection process for simplicity.

The automatic techniques we have developed can be applied to any BCG sample, but the optimal border needs to be adapted and calibrated using the imaging data from which the parent sample was derived. The calibration can be performed using a sub-sample of visually-classified BCGs, and then automatically applied to the complete sample using the structural parameters determined from standard single-Sérsic fits.

A β value needs to be chosen depending on whether we are more interested in the completeness of the cD sample or in its purity, but we suggest that $\beta = 1.25$ represents a reasonable compromise (see Section 5.3). Furthermore, it is important to remember that this method works better at selecting a sample of cD galaxies rather than a sample of non-cDs.

5.2 Distance to the optimal border

It is informative to explore the distribution of the points in the $\log R_e$–$\log RFF_{1c}$ plane (Fig. 10) in terms of their minimum (perpendicular) distance to the optimal border. We define the distance from each point to the optimal border as

$$D = \sqrt{\left(\frac{\Delta \log RFF_{1c}}{\sigma_{\log RFF_{1c}}}\right)^2 + \left(\frac{\Delta \log R_e}{\sigma_{\log R_e}}\right)^2}, \quad (8)$$

where $\Delta \log RFF_{1c}$ is the difference in $\log RFF_{1c}$ between the data point and the optimal border, and $\sigma_{\log RFF_{1c}}$ is the dispersion in $\log RFF_{1c}$ computed for all the points. $\Delta \log R_e$ and $\sigma_{\log R_e}$ have a similar meaning but for $\log R_e$. Note that, because the units of the x- and y-axes are different, the distance is measured in units of the scatter of each parameter. For each point, the minimum distance D_{min} can be then determined. Fig. 12 shows the distribution of these minimum distances for the different morphologies. As expected, the vast majority (> 80 per cent) of the cDs show positive distances (they are above the optimal border line) while most of the ellipticals have negative ones. Under 20 per cent of the cDs spill over to the negative region, severely contaminating the non-cD sample, while a few ellipticals weakly contaminate the cD region. The measurement errors in $\log R_e$ (~ 0.16) and $\log RFF_{1c}$ (~ 0.13) result in distance errors on the order of 0.7 in this metric. This contributes to the cDs' 'spillover', but does not completely explain it. Reducing the measurement errors would certainly improve the performance of our method, but it would never make it perfect.

Interestingly, the spiral and S0 BCGs are quite well separated: the former show mostly positive distances while the later have mostly negative ones. This is mainly due to spirals having generally larger RFF_{1c} values because the spiral arms and star-forming regions are not included in the Sérsic models, while the S0s are smoother. This clear separation provides a possible way to separate spiral and S0 galaxies, but this needs to be further tested with large disc samples.

Another interesting result is that BCGs classified as pure and uncertain cDs (e.g. cD/E) have very different minimum distance distributions (Fig. 13, top panel). About half of the cD/E BCGs have negative distances (i.e. are on the wrong side of the border), but only $\simeq 20$ per cent of the pure cDs do. Most of the spillover of the pure cDs into the negative region, however, can be explained by the measurement errors. It should be noticed that the difficulties inherit in the visual morphological classification are directly reflected in
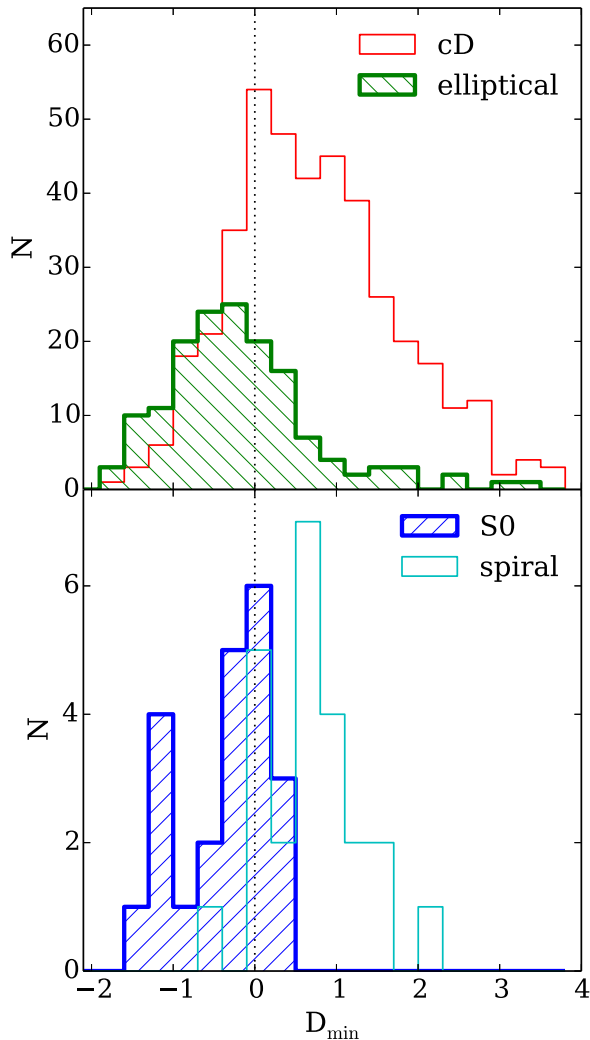
Figure 12. Distribution of the minimum distances to the optimal border shown in Fig. 10 for the cD and elliptical BCGs (top panel) and the spiral and S0 BCGs (bottom panel). Positive and negative distances correspond to points above and below the optimal border line, respectively.
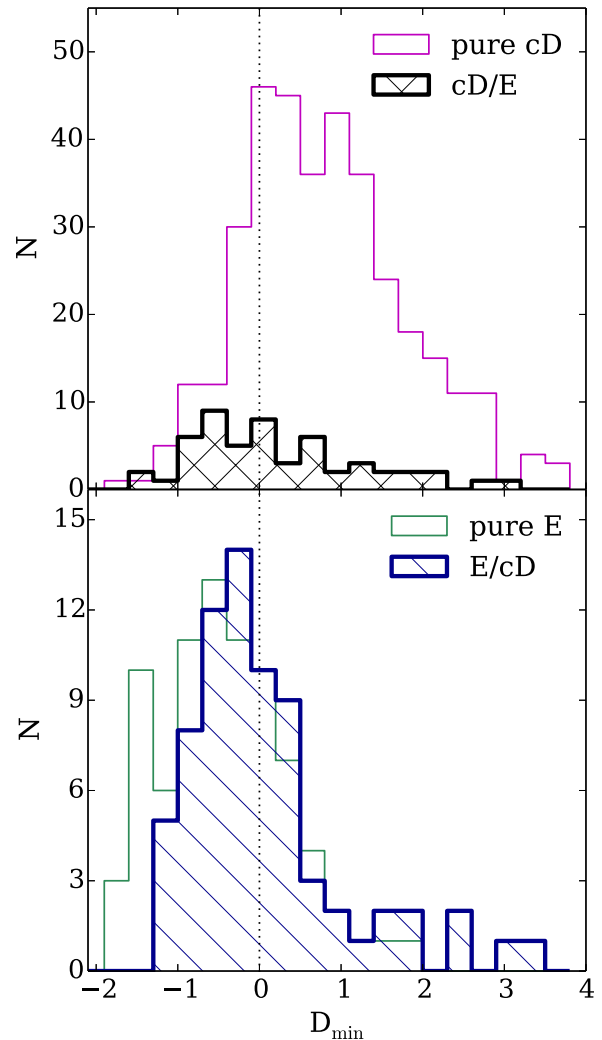
Figure 13. Distribution of the minimum distances to the optimal border shown in Fig. 10 for the pure cD BCGs and cD/E BCGs (top panel). The bottom panel shows the corresponding histograms for pure E BCGs and E/cD BCGs.

the structural parameters: when the visual classifier is certain that a BCG is a cD, its structural parameters almost always confirm it, while in uncertain cases (e.g. cD/E) the structural parameters reflect this uncertainty. Similar conclusions can also be obtained from the pure elliptical BCGs and uncertain ones (e.g. E/cD), as shown in the bottom panel of Fig. 13.

This analysis confirms the visual impression in terms of the BCG structure that there is a continuous distribution in the properties of the BCG extended envelopes, ranging from undetected (pure E class) to clearly detected (pure cD class), with the intermediate classes (E/cD and cD/E) showing increasing degrees of envelope presence. This continuous distribution in envelope detectability is reflected quantitatively in the structural parameters of the BCGs, by the minimum distance to the optimal border providing some indication of the relative importance of the envelope.

5.3 Effect of the β parameter

In the *F*-score definition, the β parameter is used to apportion weight to the completeness and the specificity. For larger values of β the

completeness is given a larger weight than the lack of contamination. Conversely, smaller values of β prioritise lack of contamination above completeness. To test how changing β affects the results of the selection process, we repeat the exercise carried out in Section 5.1 but using $\beta = 2.0$ and $\beta = 0.5$ in the determination of the optimal border.

Fig. 14 shows the optimal border for $\beta = 2.0$ (upper panel) and $\beta = 0.5$ (lower panel). It is clear that the β parameter has a decisive impact on the selection of potential cD galaxies. As shown in the upper panel, when compared to the $\beta = 1.25$ results, 11 per cent more galaxies are correctly identified as cDs, significantly increasing the completeness. The price paid is that the specificity goes down from 61 to 46 per cent since more non-cD BCGs are included. Conversely, in the lower panel ($\beta = 0.5$) the selected cD sample is purer ($p = 0.85$), but at the expense of completeness, with 20 per cent fewer cD galaxies selected when compared with the $\beta = 1.25$ result.

With $\beta = 2.0$, the contamination of the cD sample by non-cDs is 23 per cent, while the contamination of the non-cD sample by cDs is 39 per cent. With $\beta = 0.5$, the corresponding values are 12 and 52 per cent, respectively. Therefore, for any value of β this selecting
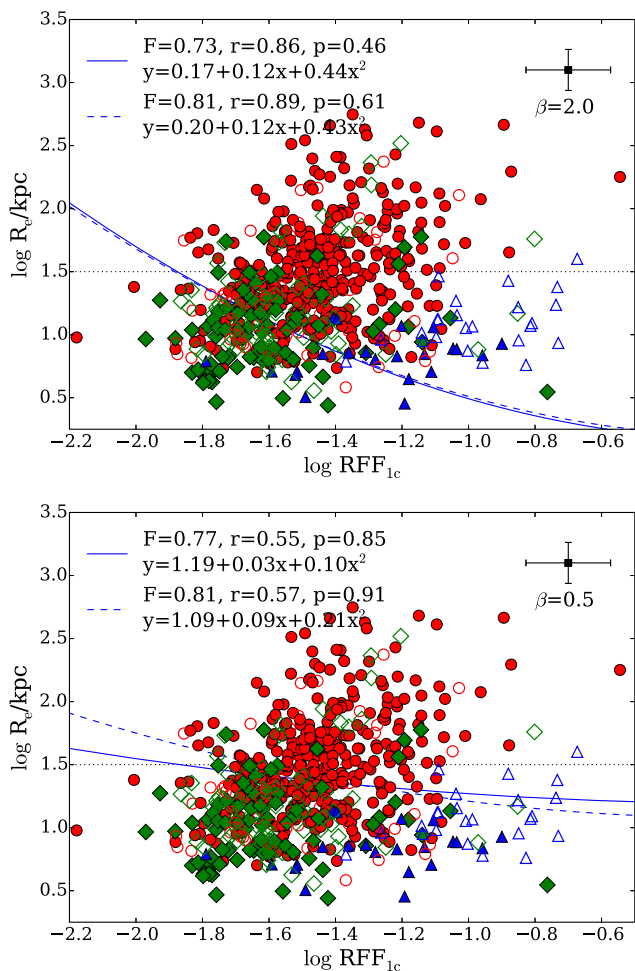
Figure 14. Illustration of the effect of β on the optimal border. The symbols, lines and legends have the same meaning as in Fig. 10 but we use $\beta = 2.0$ for the upper panel and $\beta = 0.5$ for the lower panel. With $\beta = 2.0$ we give more weight to the completeness than to the lack of contamination. When using $\beta = 0.5$, the lack of contamination is given more importance than achieving higher completeness. The choice on β depends on the aims of the specific research.

technique is cleaner and more effective at selecting cD galaxies than at selecting non-cD BCGs.

As before, if we consider a cleaner sample that contains only pure cD and pure elliptical BCGs, the optimal border (blue dashed curve) does not change significantly, but the *F*-score value, the completeness *r* and the specificity *p* improve. However, we have argued that this does not represent a realistic scenario.

We conclude that $\beta = 1.25$ represents a good compromise, as its optimal border picks up a cD galaxy sample reasonably complete, and with relatively small contamination. However, no single value of β can be considered to be 'correct' and needs to be set according to the scientific goals of the study.

6 CONCLUSIONS

In this paper, we have analysed a well-defined sample of 625 low-redshift BCGs published in L07 with the aim of linking their morphologies to their structural properties. We morphologically classified the BCGs using SDSS *r*-band images and found that over half of them ($\sim$57 per cent) are pure cD galaxies and pure ellipti-

cal BCGs constitute $\sim$13 per cent of the sample. The intermediate classes (mostly cD/E or E/cD) account for $\sim$21 per cent. It suggests a continuous distribution in the properties of the BCG extended envelopes, ranging from undetected (pure E class) to clearly detected (pure cD class), with the intermediate classes (E/cD and cD/E) showing increasing degrees of envelope presence. We found this continuous distribution in envelope detectability is reflected quantitatively in the structural parameters of the BCGs. There is also a minority of BCGs that are neither cD nor elliptical. About 7 per cent are disc galaxies (spirals and S0s, in similar proportions) and the rest ($\sim$2 per cent) are in merging (see Appendix A).

In order to link the morphologies of the BCGs to their structural properties, we have fitted the BCGs light distributions with the SDSS *r*-band images using one-component (Sérsic) and two-component (Sérsic+Exponential) models. We first characterized how well the models fit the target BCG by using two quantitative diagnostics. One diagnostic is the residual flux fraction (RFF), which measures the fraction of the galaxy flux presenting in the residual images after subtracting the models. The other diagnostic is the reduced χ_ν^2. We concluded that generally it is very difficult to find a robust diagnostic to decide, in a statistic way, whether a one-component or a two-component model is preferred for BCGs, especially for cD galaxies. Since there is no evident improvement by using two-component model fits, our other conclusions rely on the one-component Sérsic fits.

From simple one-component Sérsic profile fits, we have found a clear link between the BCGs morphologies and their structures, and claimed that a combination of the best-fitting parameters can be used to separate cD galaxies from non-cD BCGs. In particular, cDs and non-cDs show very different distributions in the R_e–RFF$_{1c}$ plane, where R_e is the effective radius and RFF$_{1c}$ is the residual flux fraction, both determined from Sérsic fits. cDs have, generally, larger R_e and RFF$_{1c}$ values than ellipticals. Therefore we found, in a statistically robust way, a boundary to separate cD and non-cD BCGs in this parameter space. BCGs with cD morphology can be selected with reasonably high completeness ($\sim$75 per cent) and low contamination ($\sim$20 per cent).

This automatic and objective technique can be applied to any current or future BCG samples which have good quality images. The method needs to be adapted and calibrated using the imaging data from which the parent sample was derived. Once calibrated with a representative sub-sample of visually-classified BCGs, this technique can be applied to the complete sample using the structural parameters determined from standard single-Sérsic fits.

In a subsequent paper (Zhao et al., in preparation), we will explore how the morphological and structural properties of BCGs are linked to other intrinsic BCG properties such as their stellar mass, and/or to the properties of their environments. These links will provide more clues to the formation history of cDs/BCGs.

including the University of Arizona, the Brazilian Participation Group, Brookhaven National Laboratory, Carnegie Mellon University, University of Florida, the French Participation Group, the German Participation Group, Harvard University, the Instituto de Astrofisica de Canarias, the Michigan State/Notre Dame/JINA Participation Group, Johns Hopkins University, Lawrence Berkeley National Laboratory, Max Planck Institute for Astrophysics, Max Planck Institute for Extraterrestrial Physics, New Mexico State University, New York University, Ohio State University, Pennsylvania State University, University of Portsmouth, Princeton University, the Spanish Participation Group, University of Tokyo, University of Utah, Vanderbilt University, University of Virginia, University of Washington, and Yale University.

REFERENCES

Barden M., Häußler B., Peng C. Y., McIntosh D. H., Guo Y., 2012, MNRAS, 422, 449
Bertin E., Arnouts S., 1996, A&AS, 117, 393
Bruce V. A. et al., 2012, MNRAS, 427, 1666
Caon N., Capaccioli M., D'Onofrio M., 1993, MNRAS, 265, 1013
Conroy C., Wechsler R. H., Kravtsov A. V., 2007, ApJ, 668, 826
de Vaucouleurs G., 1948, Ann. Astrophys., 11, 247
Donzelli C. J., Muriel H., Madrid J. P., 2011, ApJS, 195, 15
Dressler A., 1984, ApJ, 281, 512
Fukugita M., Shimasaku K., Ichikawa T., 1995, PASP, 107, 945
Gonzalez A. H., Zabludoff A. I., Zaritsky D., 2005, ApJ, 618, 195
Graham A. W., Driver S. P., Petrosian V., Conselice C. J., Bershady M. A., Crawford S. M., Goto T., 2005, AJ, 130, 1535
Guo Y. et al., 2009, MNRAS, 398, 1129
Häussler B. et al., 2007, ApJS, 172, 615
Hopkins P. F., Cox T. J., Dutta S. N., Hernquist L., Kormendy J., Lauer T. R., 2009, ApJS, 181, 135
Hoyos C. et al., 2011, MNRAS, 411, 2439
Hoyos C. et al., 2012, MNRAS, 419, 2703
Huang S., Ho L. C., Peng C. Y., Li Z.-Y., Barth A. J., 2013, ApJ, 768, L28
Huertas-Company M. et al., 2013, MNRAS, 428, 1715

Johansson P. H., Naab T., Ostriker J. P., 2012, ApJ, 754, 115
Kron R. G., 1980, ApJS, 43, 305
Lani C. et al., 2013, MNRAS, 435, 207
Lauer T. R., Postman M., 1992, ApJ, 400, L47
Liu F. S., Xia X. Y., Mao S., Wu H., Deng Z. G., 2008, MNRAS, 385, 23
Lugger P. M., 1984, ApJ, 286, 106
Miller C. J. et al., 2005, AJ, 130, 968
Oegerle W. R., Hill J. M., 2001, AJ, 122, 2858
Oser L., Ostriker J. P., Naab T., Johansson P. H., Burkert A., 2010, ApJ, 725, 2312
Patel P., Maddox S., Pearce F. R., Aragón-Salamanca A., Conway E., 2006, MNRAS, 370, 851
Peng C. Y., Ho L. C., Impey C. D., Rix H.-W., 2002, AJ, 124, 266
Peng C. Y., Ho L. C., Impey C. D., Rix H.-W., 2010, AJ, 139, 2097
Petrosian V., 1976, ApJ, 209, L1
Press W. H., Spergel D. N., 1988, ApJ, 325, 715
Schombert J. M., 1986, ApJS, 60, 603
Seigar M. S., Graham A. W., Jerjen H., 2007, MNRAS, 378, 1575
Sérsic J. L., 1963, Bol. Asociacion Argentina Astron. La Plata Argentina, 6, 41
Shen S., Mo H. J., White S. D. M., Blanton M. R., Kauffmann G., Voges W., Brinkmann J., Csabai I., 2003, MNRAS, 343, 978
Taylor-Mager V. A., Conselice C. J., Windhorst R. A., Jansen R. A., 2007, ApJ, 659, 162
van der Wel A. et al., 2012, ApJS, 203, 24
van der Wel A. et al., 2014, ApJ, 788, 28
van Rijsbergen C. J., 1979, Information Retrieval, 2nd edn. Butterworth-Heinemann, Newton, MA
von der Linden A., Best P. N., Kauffmann G., White S. D. M., 2007, MNRAS, 379, 867 (L07)
Whiley I. M. et al., 2008, MNRAS, 387, 1253
York D. G. et al., 2000, AJ, 120, 1579

APPENDIX A: DATA TABLE

Table A1 contains the main properties of the BCGs discussed in this paper. The full table is published electronically.

Table A1. Properties of the BCG sample. Columns (1) and (2) provide galaxy identifications, where ID2 is the SDSS-C4 number <SDSS-C4 NNNN> and ID3 is the SDSS C4_2003 number, <SDSS-C4-DR3 NNNN>, as given in Simbad (von der Linden et al. 2007). Columns (3) and (4) give the right ascension and declination in degrees. Column (5) gives the redshift and column (6) the velocity dispersion of the cluster. Columns (7), (8), (9), and (10) contain the effective radius, Sérsic index, residual flux fraction, and reduced χ^2 derived from the single-Sérsic fits (see the text for details). Column (11) gives the visual morphological classification of the BCGs. Column (12) contains some comments from the classifier.

ID2 (1)	ID3 (2)	RA deg (3)	DEC deg (4)	z (5)	σ_{cl} km s^{-1} (6)	$\log R_{e,\,1c}$ kpc (7)	n_{1c} (8)	RFF_{1c} (9)	χ^2_{1c} (10)	Type (11)	Comments (12)
1011	1013	227.107 346	−0.266 291	0.091	748	1.527	5.38	0.081 90	1.752	cD	Clear halo; perhaps interacting
1023	1025	153.409 478	−0.925 413	0.045	790	1.908	6.25	0.050 52	1.374	cD	Clear halo; interacting with fainter galaxies
1064	1075	153.437 067	−0.120 224	0.094	875	1.312	4.49	0.026 48	1.086	E/cD	
–	1027	191.926 938	−0.137 254	0.088	1020	1.063	4.42	0.065 94	1.903	E	Interacting/merging with bright early-type
–	1389	202.337 884	0.749 685	0.080	853	1.044	6.02	0.019 90	1.087	E/cD	Faint/small halo
2040	2050	17.513 187	13.978 117	0.059	759	2.408	9.77	0.041 22	1.224	cD	Several brightish companions
1052	1058	195.719 058	−2.516 350	0.083	749	1.627	4.89	0.046 94	1.455	cD	Multiple merger
1034	1036	192.308 670	−1.687 394	0.085	771	0.977	4.86	0.021 02	1.115	E	
1041	1044	194.672 887	−1.761 463	0.084	771	2.318	5.64	0.050 23	1.280	cD	Very large, elongated halo; some faint companions
–	1126	192.516 071	−1.540 383	0.084	878	2.039	9.12	0.045 20	1.348	cD	Interacting with faint companions
3002	3004	258.120 056	64.060 761	0.080	1156	1.667	4.81	0.025 61	0.991	cD	
3096	3283	135.322 540	58.279 747	0.098	756	1.866	6.96	0.055 35	1.144	cD	Merging with bright companion

Table A1 – *continued*

ID2 (1)	ID3 (2)	RA deg (3)	DEC deg (4)	z (5)	σ_{cl} km s^{-1} (6)	$\log R_{e,1c}$ kpc (7)	n_{1c} (8)	RFF_{1c} (9)	χ^2_{1c} (10)	Type (11)	Comments (12)
1045	1048	205.540 176	2.227 213	0.077	828	0.883	2.52	0.106 89	11.280	E/cD	Multiple merger
1003	1004	184.421 356	3.655 806	0.077	966	1.753	4.75	0.052 33	1.225	cD/E	Interacting/merging with early-type
–	1456	173.336 242	2.199 054	0.099	746	1.696	8.09	0.025 73	1.128	cD	
1053	1061	228.220 703	4.514 004	0.038	789	0.875	7.54	0.017 49	1.074	cD	
2163	2074	314.975 446	−7.260 758	0.079	765	1.231	8.03	0.044 81	1.315	E/cD	
2002	2002	358.557 007	−10.419 200	0.076	812	2.660	11.12	0.038 32	1.201	cD	Many faint and brightish companions
2006	2013	10.460 272	−9.303 146	0.056	903	1.433	1.62	0.041 40	1.477	cD	Several faint companions
1355	1460	175.554 108	5.251 709	0.097	1074	0.952	5.30	0.015 57	1.052	cD	Interacting with faint galaxy; faint but clear halo
1058	1069	184.718 166	5.245 665	0.076	721	1.988	7.98	0.041 44	1.251	cD	Interacting with faint galaxies
1002	1002	159.777 581	5.209 775	0.069	800	1.740	8.40	0.038 38	1.321	cD/E	Clear halo
–	1276	183.271 286	5.689 677	0.081	729	0.995	5.30	0.021 42	1.151	E	
1039	1042	228.808 792	4.386 210	0.098	857	1.800	8.77	0.043 65	1.205	E/cD	Some halo? faint companions
–	3332	124.471 428	40.726 395	0.063	802	1.463	6.40	0.081 25	2.639	SB0	
3011	3028	204.034 694	59.206 401	0.070	872	2.120	7.86	0.081 72	1.556	cD	Several faint companions
1001	1001	208.276 672	5.149 740	0.079	746	1.820	7.85	0.027 20	1.128	E/cD	
3004	3012	255.677 078	34.060 024	0.099	1127	1.717	3.54	0.084 33	1.949	cD	Late merger?
–	3094	254.933 115	32.615 319	0.098	875	1.291	3.50	0.028 78	1.069	cD	Very faint companions
–	1066	202.795 126	−1.730 259	0.085	814	1.942	9.09	0.036 53	1.161	E/cD	Interacting/merging with bright galaxy and fainter one
–	2214	321.599 487	10.777 511	0.095	741	0.818	3.98	0.022 60	1.199	E	
2096	2109	359.836 166	14.670 211	0.093	786	1.161	6.56	0.035 72	1.242	cD/E	
2085	2085	334.197 449	−9.724 778	0.094	806	0.779	3.43	0.028 61	1.348	cD	
2027	2035	4.177 309	−0.445 436	0.065	1084	1.436	8.89	0.024 17	1.168	cD	Several companions
–	3084	118.360 820	29.359 459	0.061	781	1.584	3.95	0.066 32	1.382	cD	Several faint and bright companions
–	3347	119.679 733	30.773 809	0.076	902	1.354	6.04	0.014 70	1.019	E/cD	
–	1283	125.745 443	4.299 105	0.095	754	2.747	10.47	0.044 83	1.094	cD	Several faintish companions
–	1039	186.878 093	8.824 560	0.090	846	1.962	6.94	0.061 00	1.965	cD	Clear halo, bright companion (dumbbell galaxy)

SUPPORTING INFORMATION

Additional Supporting Information may be found in the online version of this article:

Table A1. Properties of the BCG sample. Columns (1) and (2) provide galaxy identifications, where ID2 is the SDSS-C4 number <SDSS-C4 NNNN> and ID3 is the SDSS C4_2003 number, <SDSS-C4-DR3 NNNN>, as given in Simbad (von der Linden et al. 2007). Columns (3) and (4) give the right ascension and declination in degrees. Column (5) gives the redshift and column (6) the velocity dispersion of the cluster. Columns (7), (8), (9), and (10) contain the effective radius, Sérsic index, residual flux fraction, and reduced χ^2 derived from the single-Sérsic fits (see the text for details). Column (11) gives the visual morphological classification of the BCGs. Column (12) contains some comments from the classifier.

(http://mnras.oxfordjournals.org/lookup/suppl/doi:10.1093/mnras/stv190/-/DC1).

Please note: Oxford University Press is not responsible for the content or functionality of any supporting materials supplied by the authors. Any queries (other than missing material) should be directed to the corresponding author for the paper.

This paper has been typeset from a TeX/LaTeX file prepared by the author.